

This is the peer reviewed version of the following article:

J. Dobrić, A. Filipović, Z. Marković, N. Baddoo, Structural response to experimental axial testing of cold-formed stainless steel equal angle columns, *Thin-Walled Structures.*, 156 (2020) 1-16.

<https://doi.org/10.1016/j.tws.2020.106986>

# Structural response to axial testing of cold-formed stainless steel angle columns

Jelena Dobrić<sup>1</sup>, Aljoša Filipović<sup>2</sup>, Zlatko Marković<sup>3</sup>, Nancy Baddoo<sup>4</sup>

<sup>1</sup> University of Belgrade, Faculty of Civil Engineering, Serbia, [jelena@imk.grf.bg.ac.rs](mailto:jelena@imk.grf.bg.ac.rs)

<sup>2</sup> University of Belgrade, Faculty of Civil Engineering, Serbia, [afilipovic@grf.bg.ac.rs](mailto:afilipovic@grf.bg.ac.rs)

<sup>3</sup> University of Belgrade, Faculty of Civil Engineering, Serbia, [zlatko@imk.grf.bg.ac.rs](mailto:zlatko@imk.grf.bg.ac.rs)

<sup>4</sup> Steel Construction Institute, United Kingdom, [n.baddoo@steel-sci.com](mailto:n.baddoo@steel-sci.com)

Corresponding author: Jelena Dobrić, [jelena@imk.grf.bg.ac.rs](mailto:jelena@imk.grf.bg.ac.rs) (phone: +381-11-3218-626)

## Highlights:

Eleven pin-ended cold-formed stainless steel equal-leg angle columns were tested.

Different buckling failure modes were systematically investigated.

Failure loads conservatively predicted by European and Australian design procedures.

# Structural response to axial testing of cold-formed stainless steel angle columns

## **Abstract**

In this paper, the structural stability and compressive capacity of pin-ended cold-formed stainless steel angle columns with different slenderness were experimentally investigated. The experimental programme was performed on press-braked lean duplex stainless steel equal-leg angle sections with nominal dimensions of  $80 \times 80 \times 4$  mm, and involved material testing, initial imperfection measurements and 11 column tests. The test setup and procedure, together with the key experimental results, axial load vs. lateral deflections, axial load vs. torsional rotations and characterised failure modes, were fully reported and analysed. The experimental observations reveal that the failure mode type, including local/torsional, flexural-torsional and flexural effects, is highly dependent on the column's slenderness and initial imperfections. The measured compressive strengths were compared with the resistance predictions determined according to European and Australia/New Zealand codified design procedures. It was found that experimentally obtained ultimate capacities are significantly higher than those calculated according to the specifications. However, the database of test results is still quite limited, and a further research is needed to amplify the data needed to enable a more precise assessment of the codified procedures.

**Key-words:** Experiment; Equal-leg angle section; Cold-formed; Flexural-torsional buckling; Flexural buckling; Stainless steel.

## 1. Introduction

The increasing use of cold-formed stainless steel angles in various applications of modern construction requires a specific methodology for their design, considering both single and built-up angle shapes. Despite the basic simplicity and adaptability of the angle shape, its asymmetry, non-coincidence of the shear centre with the section's centroid, negligible warping resistance and low torsional stiffness cause complex structural responses of angle members under axial compression. In general, cold-formed equal-leg angle columns exhibit two major buckling modes or their combination, depending on the cross-section slenderness, overall slenderness and boundary conditions: flexural buckling (FB) about the minor cross-section principal axis in the high and intermediate slenderness ranges and flexural-torsional buckling (FTB) about the major cross-section principal axis in the intermediate and low slenderness ranges. Besides, due to the low torsional rigidity, short equal-leg angle columns could be susceptible to the torsional buckling (TB) mode whose failure shape corresponds to the local buckled shape of a slender equal-leg angle section. However, the consequence of the non-coincidence of the shear centre with the section's centroid makes the torsion buckling never critical in equal-leg angle columns.

Evaluating the possibility for FB- or FTB-governed failure modes is not straightforward, especially in the case of slender equal-leg angle sections. Due to the localized redistribution of stresses and deformations after elastic local buckling (LB), axially compressed angle section loses the stiffness and effective section properties. As a result, the effective centroid shifts along the axis of symmetry towards the corner, leading to interaction between the initial axial load and additional uniaxial bending. Furthermore, the inevitable presence of initial imperfections of geometry and loading of a real column additionally affects its structural response. Hence, simultaneous effects of the effective centroid shift, end eccentricity of loading and amplitude of geometric imperfections on column buckling strength should be considered. Because the cross-section is asymmetric, the combination of axial load with minor-axis bending results in a nonuniform distribution of axial stresses along the angle legs. The distribution pattern strongly depends on the direction of total eccentricity along the axis of symmetry (major-axis of an equal angle section)—towards the tips of the legs or to the corner—one causing compressive yielding of the leg tips, the other causing compressive yielding of the section corner. This impact is more significant in pin-ended columns than in fixed-end

columns, because of the ability of fixed-ended boundary conditions to prevent additional bending caused by the shift of the effective centroid, otherwise induced in pinned-ended columns. It should be noted also that an increase of the leg width-to-thickness ratio increases the tendency of the angle to rotate, thus, potentially leading to FTB failure, in the entire overall slenderness range.

The knowledge gained through theoretical and experimental work on cold formed carbon steel (CFS) angle columns represents an important benchmark for studying cold-formed stainless steel (CFSS) angle columns. Basically, considering cross-sectional geometry and impact of initial imperfections, the structural behaviours of equivalent CFSS and CFS angle columns are quite similar. However, pronounced material nonlinearities of stainless steel grades, which differ among the stainless steel alloy families, significantly affect the buckling resistance of CFSS columns.

The buckling response and design of CFS angle columns has been, and continues to be, the subject of extensive research projects across the globe. The following relevant references deserve to be mentioned here. Peköz (1986) [1] thoroughly studied available test data and found the significant influence of initial sweep (out-of-straightness) of an angle column on its compression resistance. The author concluded that the sweep in the plane of symmetry toward the section corner significantly decreases column's buckling resistance than the sweep in opposite direction. Based on this outcome, the author suggested to account for an additional moment of  $P \cdot L / 1000$  (where  $P$  is the compressive axial load and  $L$  is the column height) about the minor-principal axis in the design of axially compressed angle members. This recommendation was introduced in the 1986 edition of the AISI Specification. Popovic et al. (1999) [2] performed a series of tests on fixed-ended and pin-ended CFS angle columns, covering both non-slender and slender sections, to study their FB and FTB response. The authors noticed that the compressive capacities of columns with slender angle sections are strongly affected by the eccentricity direction at the columns' ends. The higher level of compressive stresses at the section's corner, caused by load eccentricity applied towards the corner, reduces the stress level at the legs' tips and leads to greater column strength in comparison with corresponding columns with eccentricity applied toward the tips of the legs. It was recommended that an additional bending moment accounting for the shift of the effective centroid—stated in the established Australian and American cold-formed specifications—should not be considered in design of columns with non-slender angle section.

Besides, the required additional bending moment caused by load eccentricity should only be applied in the design of slender sections. Consequently, clarification was made in the next edition of the AISI and AS/NZS specification. Popovic et al. (2001) [3] conducted experiments on 11 pin-ended CFS columns with slender equal-leg angle sections under three different eccentricity conditions to provide strong evidence for interaction of local and global column buckling and investigate their sensitivity to loading eccentricity. Based on the obtained results, the authors proposed that the procedure for the FTB failure mode should be omitted from the codified method stated in Australian and American specifications and only minor-axis FB should be considered. Young (2004) [4] conducted experimental tests on axial compressed fixed-ended plain angle columns produced by press-braking from high strength structural steel sheets. The new design equations both slender and non-slender angle sections were proposed. It was recommended that the proposed design equations should be used only for FB, whereas the elastic TB and FTB stress may be ignored in design calculations. It was also recommended that the additional moment of  $P \cdot L / 1000$  can also be ignored in calculating the column design strengths for both slender and non-slender CFS plain angle sections. Ellobody and Young (2005) [5] reported an extensive numerical parametric study on CFS angles compressed between fixed ends over different column lengths to evaluate existing design recommendations. The numerical results emphasized the conservatism of the established codified procedures and showed good agreement with the predictions obtained by the new design equations proposed in previous investigation [4]. Rasmussen (2005) [6] developed a new design method for pin-ended CFS columns with slender equal-leg angle sections loaded through the gross section centroid or with an eccentricity of  $L / 1000$  from the gross section centroid (where  $L$  is the column height). The design procedure, based on the beam–column approach, excludes the torsional stresses in determining the compression and bending member resistance and considers the shift of the effective centroid taking into account the actual post-buckling stress distribution. The reason for ignoring global TB is that it is already accounted for in the LB reduction in determining the effective cross-section area. In parallel, the author proposed a simple design model for centrally compressed angles which applies a reduction factor to account for the effect of an additional bending moment caused by the shift in the effective neutral axis and does not include the use of an interaction equation. Chodraui et al. (2006) [7] performed an accuracy assessment of the predicted buckling resistances of centrally loaded CFS equal

angle columns determined by codified procedures based on the Effective Width Method (EWM) and Direct Strength Method (DSM) using experiments, numerical methods and imperfection sensitivity studies. Contrary to previous findings, the authors' results indicated that the design approach which ignores TB as an global mode may lead to unconservative predictions. It was concluded that the established codified procedures should treat LB and TB as both a local-plate mode and an overall-torsional mode. Dinis and Camotim (2015) [8] developed a new design approach for thin-walled fixed-ended and pin-ended angle columns, based on DSM, which includes the use of length-dependent flexural–torsional strength curves and considers the interaction between two global modes, FTB and FB. Landesmann et al. (2017) [9] performed an experimental investigation of CFS pin-ended equal angle columns. The geometry of specimens was chosen to provide the transition from FTB to FB mode. Based on experiments and a subsequent numerical parametric study, an assessment of the proposed DSM-based design approach was carried out, which was shown to offer a high level of accuracy in the prediction of strengths of CFS equal-leg angle columns. Although extensive efforts have been devoted to determining the compressive capacity of CFS angle columns, the design of compressed CFSS angle columns, including both experimental and numerical research, has attracted less attention. Among other types of cross-sections, Kuwamura (2003) [10] performed experiments on 12 cold-formed stainless steel column specimens with short lengths comprising plain equal-leg angles made of austenitic EN1.4301 and EN1.4318 grades. Zhang et al. (2019) [11] experimentally and numerically investigated FTB of fixed-ended cold-formed austenitic stainless steel equal-leg angle columns. The obtained results were used to evaluate current EN 1993-1-4 [12], SEI/ASCE-8 [13] and AS/NZS 4673 [14] specifications and, in parallel, the DSM-based design approach [9], for FTB predictions. Comparative analysis indicates that the effective width method employed in codified design procedures leads to a high level of conservatism and data scatter, whereas the DSM-based design method, initially developed for CFS angles, significantly improves design accuracy, although with unsafe strength predictions for a significant number of data. Along with the efforts on determining the FTB capacity of cold-formed stainless steel angle columns, their structural responses under FB actions require more comprehensive experimental research work. For the case

of cold-formed stainless steel equal angle columns with pin-ended boundary conditions, experimental studies are scant.

In view of this, our paper presents an experimental investigation of the structural responses of pin-ended cold-formed equal-leg angle columns made from a lean duplex stainless steel grade. Eleven EN 1.4162 specimens with three different lengths, namely, short (240 mm), intermediate (1000 mm) and long (2000 mm), were tested under axial compression load to characterize the failure modes and column strength. The experimental results including LB, FTB and FB were fully reported and then thoroughly analysed and discussed. The current European [12] and Australian/New Zealand [14] specification approaches including the EWM were used to compare experimentally determined specimen strengths with their design predictions, showing safe but conservative results, especially for FTB.

The presented results are a part of an on-going comprehensive investigation addressing cold-formed, hot-rolled and laser-welded stainless steel equal-leg angle columns with pin-ended boundary conditions, conducted at the University of Belgrade, Faculty of Civil Engineering [15], [16]. The investigation includes experiments and geometric and material nonlinear finite element failure analyses, proposing design procedures that take into account the cross-section slenderness, material non-linearity and initial structural imperfections caused by different production processes.

## **2. Experimental programme**

### **2.1. General**

In order to investigate the structural behaviour of CFSS equal-angle columns, a series of tensile material tests, compressive stub column tests and global buckling tests were conducted. The tests were performed on plain press-braked angles from high strength lean-duplex stainless steel grade EN 1.4162 having nominal yield stress of 480 MPa [17]. Each specimen in the experimental program has a designation of ACF  $80 \times 80 \times 4 - L - X$  where the first letters “ACF” indicate angle cold-formed section, followed by the nominal section sizes in millimetres (leg width  $b \times$  leg width  $b \times$  thickness  $t$ ), “L” is the length of the specimens and “X” is a sequential number from 1 to 4, which relates to the repeated specimens within one tested group. The nominal internal corner radius of the section,  $r_i$ , was adopted to be equal to  $3 \cdot t = 12$  mm. The nominal flat leg width-to-thickness ratio is equal to 17, which classifies specimens’ angle-sections as slender (Class 4) [12].

The lengths of specimens were selected to cover a wide-ranging set of global column slenderness in order to meet different performance levels of structural behaviour: elastic LB of short specimens, and coupled FTB–LB and FB-LB failure modes in the case of intermediate and long specimens, respectively. This section summarizes the experimental procedures, description of the test set-up and instrumentations, and the relevant test data.

## 2.2. Material properties

The basic material of all tested angle columns was lean-duplex stainless steel grade EN 1.4162 (UNS S32101) with the steel name X2CrMnNiN21-5-1 [17]. The stainless steel alloy was supplied in hot-rolled sheets with a nominal thickness of 4.0 mm. The tensile tests were performed on coupons extracted from the basic flat sheet material and final press-braked angle sections (ACF  $80 \times 80 \times 4$ ,  $r_1 = 12$  mm) under strain-control according to the requirements of EN ISO 6892-1 [18]. The tests were carried out on an AG-Xplus Universal Testing Machine (Shimadzu, Japan) with a capacity of 300 kN. Five flat coupons were taken from the steel strip: two in the longitudinal direction and three in the transverse direction relative to the strip rolling direction. In order to indicate the enhancement of material strength due to cold-working, four coupons were longitudinally cut from the angle-section: two coupons were taken from the middle of a leg, and two from the corner regions. The longitudinal axis of the specimens was aligned with the strip rolling direction. All coupons were cut by a water jet cutter to decrease heating of material during their preparation. The flat coupons were 12.5 mm wide, whereas the corner coupons were cut within the boundary of the internal radius of the cross-section's corner regions. The calibrated extensometers with gauge lengths,  $L_0$ , of 50 and 25 mm were used to measure the longitudinal strains of the flat and corner coupons, respectively. The adopted strain rates were 0.1 mm/min for the initial part of the test up to approximately 1% total strain after which it was increased to 2.0 mm/min.

Fig. 1a shows the material tensile coupon test setup. The obtained engineering stress–strain curves are provided in Fig. 1b along with the location of the coupons in the angle section and flat coupons' dimensions. Average values of key mechanical properties are summarized in Table 1, in which  $E$  is the modulus of elasticity,  $f_y$  is yield strength taken as the 0.2% proof stress,  $\sigma_{0.01}$ ,  $\sigma_{0.05}$ ,  $\sigma_{1.0}$  are different proof stresses,  $f_u$  is the ultimate tensile strength,  $\varepsilon_u$  is the strain corresponding to the ultimate tensile strength,  $\varepsilon_f$  is the total strain

at fracture, and  $n$  and  $m$  are the strain hardening parameters utilised in the Ramberg–Osgood material model for nonlinear metallic materials [19].

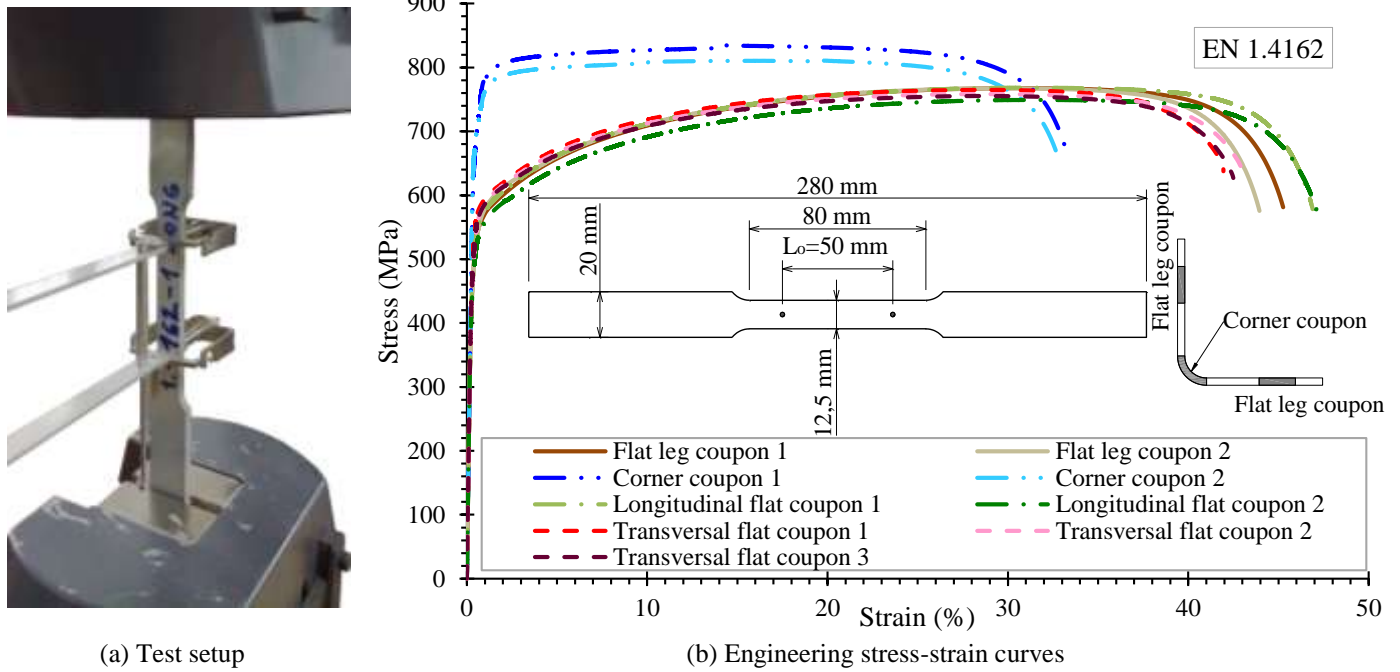


**Fig. 1.** Tensile coupon test.

Based on test data (see Table 1), the average yield strength measured on transverse coupons, exceeds the specified nominal values of 480 MPa by a margin of 12.5%. The longitudinal yield strength value is about 6% lower than the transverse value. Additionally, press-braking, as a cold-forming method, leads to a significant strength enhancement at the corner regions; the yield strength is about 38% greater than the yield strength of the flat strip material. However, there is no noticeable impact on the improvement of material properties in the flat legs of the angle section.

**Table 1.** Average measured material properties obtained from tensile coupon tests.

Coupon	$f_y$ (N/mm <sup>2</sup> )	$\sigma_{0.01}$ (N/mm <sup>2</sup> )	$\sigma_{0.05}$ (N/mm <sup>2</sup> )	$\sigma_{1.0}$ (N/mm <sup>2</sup> )	$f_u$ (N/mm <sup>2</sup> )	$E$ (N/mm <sup>2</sup> )	$\epsilon_u$ (%)	$\epsilon_f$ (%)	Strain hardening parameters	
									$n$	$m$
Longitudinal flat coupons / sheet material	508	357	432	578	759	199348	31	47	8.0	3.1
Transverse flat coupons / sheet material	540	384	461	601	759	199605	27	43	8.0	2.9
Flat leg coupons	517	350	424	588	768	197445	31	45	7.9	3.0
Corner coupons	703	586	641	788	823	199905	17	33	11.0	13.1

### 2.3. Measurements of geometric imperfections

Measurements of specimen dimensions and quantification of initial geometric imperfections were performed using a multiplanar laser tracker system. A commercial laser tracker was used, namely the Leica Absolute Tracker AT960 (Hexagon Manufacturing Intelligence, UK), designed as a fully portable dynamic system

with six degrees of freedom. A spherically mounted retroreflector (SMR) was used as a measurement target device of the system. Six measurement parameters completely describe the target device in relation to the laser tracking system. These are three position parameters ( $\Delta x$ ,  $\Delta y$  and  $\Delta z$ ) and three orientation parameters (pitch, yaw and roll). Together, they comprise the Six Degrees of Freedom principle.

These parameters are determined by the Leica Absolute Tracker. With optical centring accuracy of  $\pm 3 \mu\text{m}$ , the SMR offers a highly accurate solution within  $15 + 6 \mu\text{m/m}$  for line-of-sight measurements. By measuring a series of points across a measurement area, the Leica Absolute Tracker can produce a measurement grid defining the target measurement surface. The density of that point-grid is also customisable, putting the operator in complete control of the balance between process speed and the level of detail that will feed into the metrology software. The obtained raw point-grid data are carefully used in post processing to obtain the desired geometric information. Specimens are placed on a support beam to minimize deflections under the specimens' self-weight. The laser tracker setup with an installed specimen is shown in Fig. 2.



**Fig. 2.** Laser tracker setup with installed specimen.

Full-field geometric information of a target specimen was achieved as a point-grid by measuring the outer surface of the specimen at multiplanes of view and registering the individual set of measurements into the same final global coordinate system. The measured segments are first registered in the global coordinate system and coloured based on deviation from nominal specimen geometry, see Fig. 3.

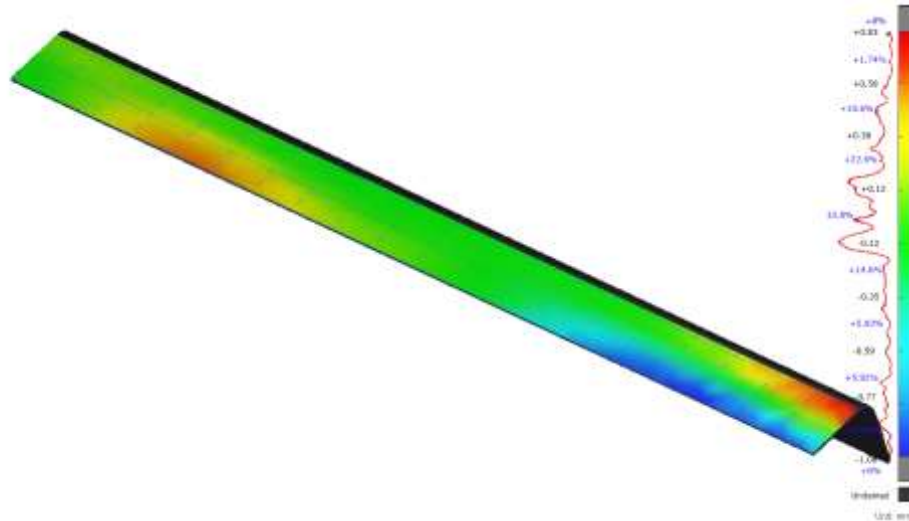


**Fig. 3.** Models reconstructed from the Leica Absolute Tracker system.

The point-grids consist of nodal points determined for each registered cross-section along the length of the specimen. Typical point-grid measurement for a specimen includes 53 points in a cross-section and 666 points along the length (> 35200 points per specimen).

The actual geometry of specimens, including cross-section dimensions and specimens' lengths was estimated as average values of corresponding geometric data derived from reconstructed point-grid measurement models. The summary of typical dimensions, including cross-section areas determined for measured dimensions, is provided in Table 2, together with comparisons with nominal specifications. For the overall dimensions, differences between the mean value of the measurement models reported here and that of nominal specifications are generally smaller than 1.6%. The coefficients of variation (CoV) range from 0.1% to 2.9%.

**Table 2.** Average measured geometrical dimensions of the specimens.

Specimens	Length $L$ (mm)	Width of	Width of	Thickness $t$ (mm)	Internal corner radius $r_i$ (mm)	Angle between legs $\beta$ ( $^\circ$ )	Cross-section area (mm <sup>2</sup> )
		leg 1 $c_1$ (mm)	leg 2 $c_2$ (mm)				
ACF $80 \times 80 \times 4 - 240 - 1$	239.6	80.4	81.4	4.0	11.9	89	607.3
ACF $80 \times 80 \times 4 - 240 - 2$	239.5	80.7	80.4	4.1	12.0	91.2	619.0
ACF $80 \times 80 \times 4 - 240 - 3$	240.8	80.2	81.1	4.1	12.0	90.6	619.8
Nominal dimensions	240.0	80.0	80.0	4.0	12.0	90	606.8
Mean value	240.0	80.4	81.0	4.0	12.0	90.2	615.4
CoV (%)	0.3	0.3	0.6	2.9	0.5	1.0	1.1
Mean value vs. nominal dimension (%)	0.0	-0.5	-1.3	0.0	0.0	-0.2	-1.4
ACF $80 \times 80 \times 4 - 1000 - 1$	999.8	80.2	79.3	4.1	12.2	90.7	612.1
ACF $80 \times 80 \times 4 - 1000 - 2$	1001.8	80.6	81.0	3.9	11.9	91	606.5
ACF $80 \times 80 \times 4 - 1000 - 3$	1002.0	80.4	81.0	4.0	12.1	90.6	605.4
ACF $80 \times 80 \times 4 - 1000 - 4$	999.0	80.7	79.6	4.1	12.0	89.1	615.7
Nominal dimensions	1000.0	80.0	80.0	4.0	12.0	90	606.8
Mean value	1000.7	80.5	80.2	4.0	12.1	90.3	609.9
CoV (%)	0.1	0.3	1.1	2.4	1.1	0.8	0.8
Mean value vs. nominal dimension (%)	0.1	0.6	0.2	0.0	0.8	-0.3	0.5
ACF $80 \times 80 \times 4 - 2000 - 1$	2002.0	80.0	81.4	4.1	11.8	91.2	620.6
ACF $80 \times 80 \times 4 - 2000 - 2$	2001.8	80.7	81.5	3.9	12.2	89.8	623.1
ACF $80 \times 80 \times 4 - 2000 - 3$	1999.4	79.8	80.8	4.0	12.1	90.5	602.2
ACF $80 \times 80 \times 4 - 2000 - 4$	2001.3	81.6	80.0	4.1	12.0	89.1	621.0
Nominal dimensions	2000.0	80.0	80.0	4.0	12.0	89	606.8
Mean value	2001.1	80.5	80.9	4.0	12.0	89.9	616.7
CoV (%)	0.1	1.0	0.9	2.4	1.4	1.0	1.6
Mean value vs. nominal dimension (%)	0.1	0.6	1.1	0.0	0.0	-1.0	1.6

Note:  $c_1$  and  $c_2$  are leg outer section widths (including external radius)

Geometric imperfections were also identified from the measurement point-grids. Local imperfections related to cross-section distortion and three key global imperfections related to bow, camber and twist were studied (see Fig. 4).

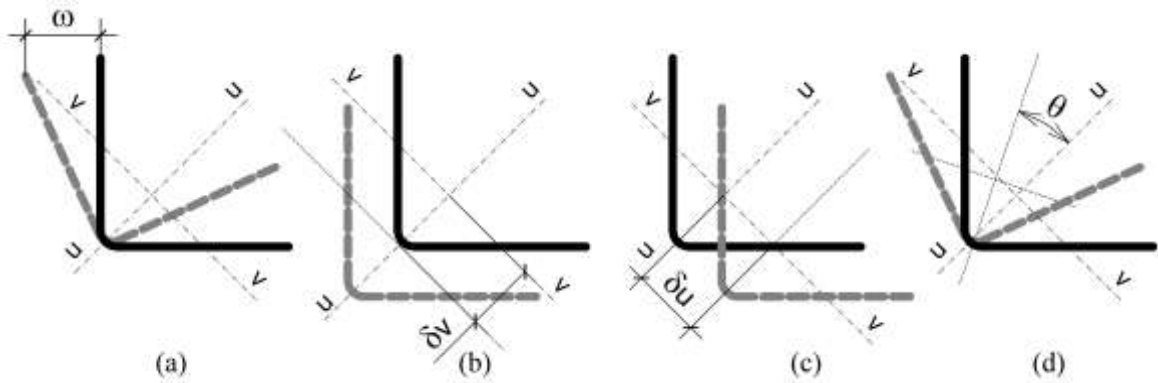


**Fig. 4.** Imperfection definition: (a) cross-section imperfection; (b) bow imperfection; (c) camber imperfection; (d) twist imperfection.

The imperfection amplitudes are calculated from the reconstructed three-dimensional point-grids acquired by the laser tracker. The distribution of local imperfections, denoted as  $\omega$ , was constructed by finding the perpendicular distances from ideal plane angle section legs (compounding a  $90^\circ$  angle) to the measured legs.

The maximum perpendicular deviation was used as local imperfection amplitude  $\omega_0$  (the local imperfection amplitude represents an extreme of the measured values for both legs). The camber imperfections, perpendicular to the major-axis ( $\delta_u$ ), and bow imperfections, perpendicular to the minor-axis ( $\delta_v$ ), are established by finding the centroid of each measured cross-section and comparing it to the nominal cross-section centroid. It was assumed that centroids at the ends of the specimen coincide with equivalent centroids obtained for nominal specimen geometry. The maximum values found from the comparisons are denoted as extreme imperfections of camber ( $\delta_{u,0}$ ) and bow ( $\delta_{v,0}$ ) imperfections, respectively. The distribution of initial twist imperfections designated as  $\theta$  and angle of twist of the entire specimen were determined by using a mid-span cross-section which was set as the null reference section. The angle of twist, defined as the difference between the two ends, was used to define the extreme twist imperfection ( $\theta_0$ ).

The distributions of measured cross-section, bow, camber and twist geometric imperfections along the length of selected specimen ACF  $80 \times 80 \times 4 - 1000 - 4$  are provided in Fig. 5.

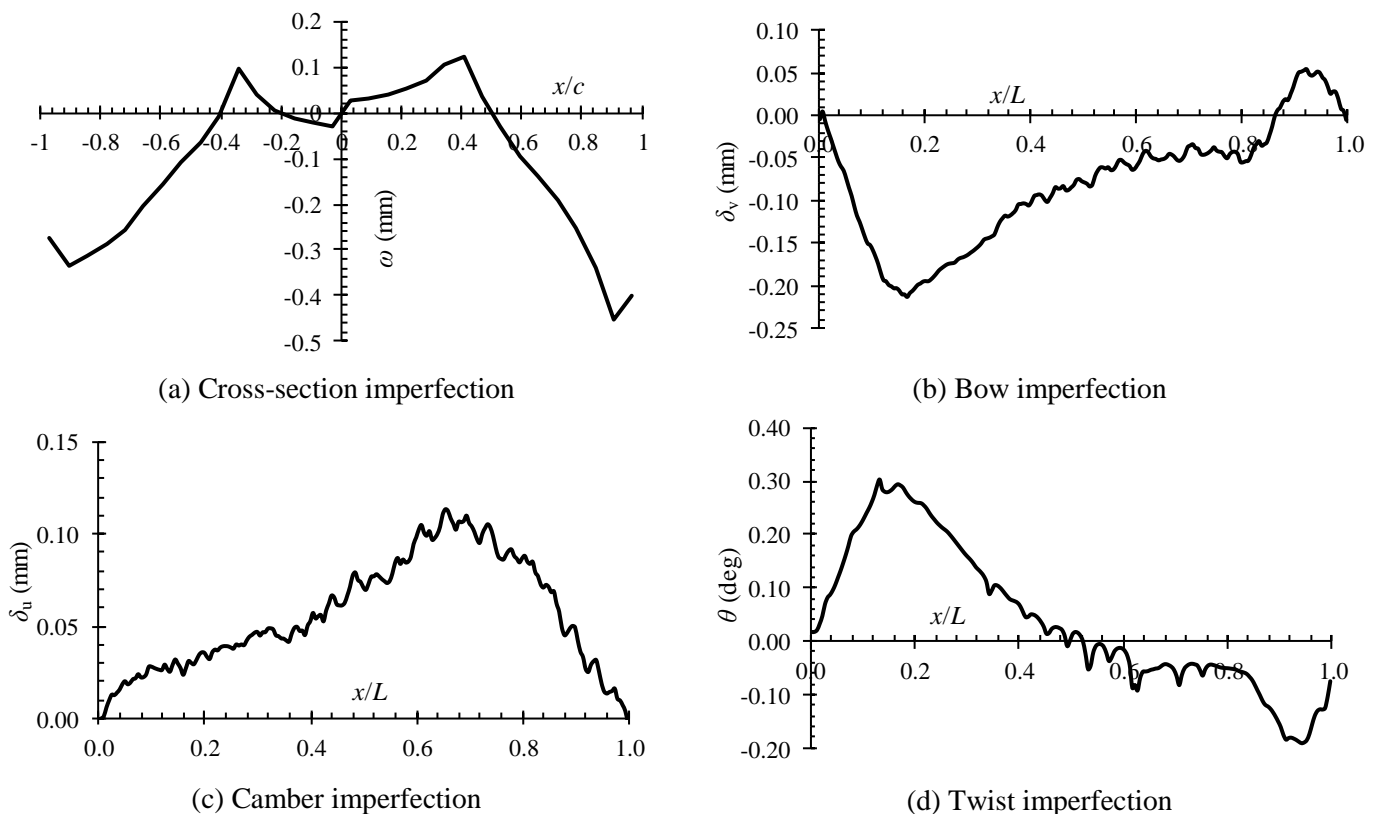


**Fig. 5.** Distributions of measured initial geometric imperfections of specimen ACF  $80 \times 80 \times 4 - 1000 - 4$ .

Table 3 summarizes the extreme values (amplitudes) of local and global initial geometrical imperfection  $\omega_0$ ,  $\delta_{0,u}$ ,  $\delta_{0,v}$  and  $\theta_0$  measured for all specimens, along with their corresponding normalized values  $\omega_0/c$ ,  $\delta_{0,u}/L$ ,  $\delta_{0,v}/L$  and  $\theta_0/L$ , respectively.

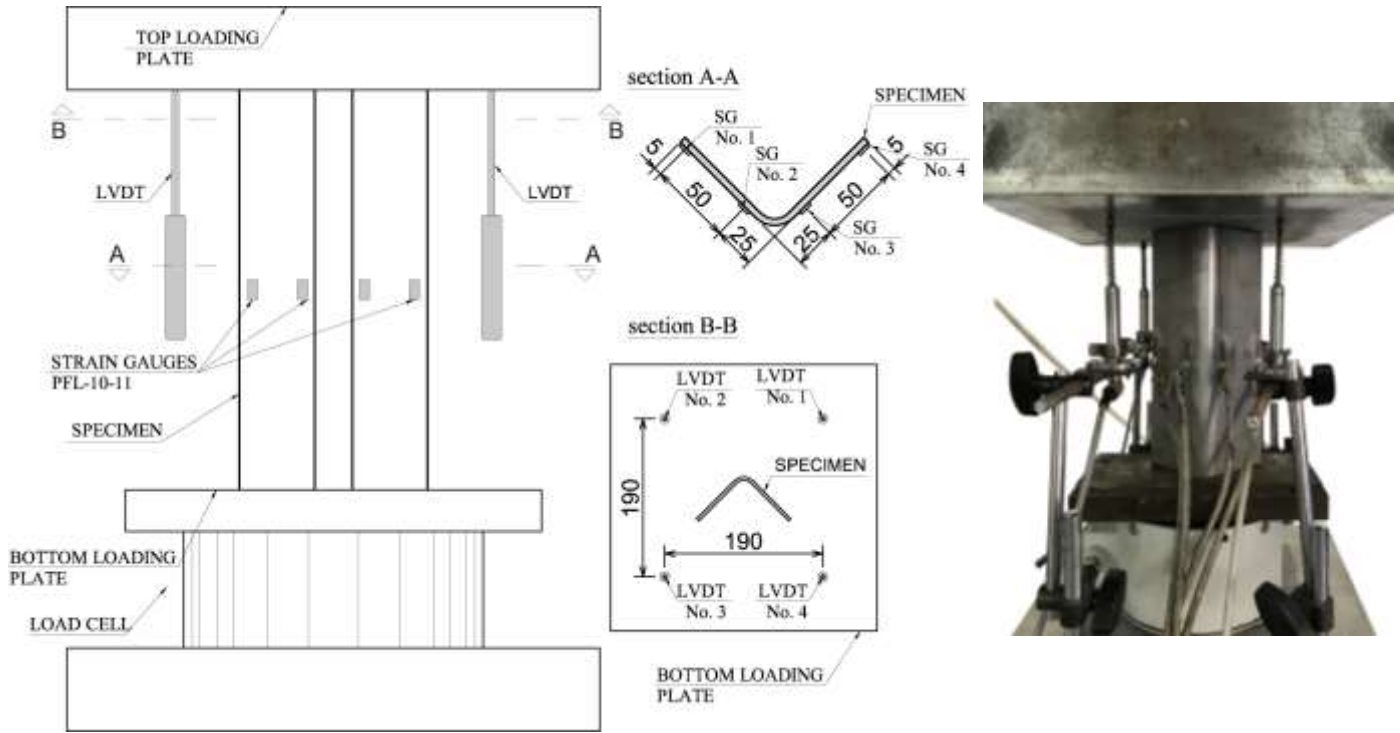
**Table 3.** Measured amplitudes of initial geometric imperfections.

Specimens	$\omega_0$ (mm)	$\omega_0/c$ (-)	$\delta_{v,0}$ (mm)	$\delta_{v,0}/L$ (-)	$\delta_{u,0}$ (mm)	$\delta_{u,0}/L$ (-)	$\theta_0$ (°)	$\theta_0/L$ (°/m)
ACF 80 × 80 × 4 – 240 – 1	0.326	$c/245$	0.031	$L/7742$	0.010	$L/24000$	0.075	0.312
ACF 80 × 80 × 4 – 240 – 2	0.283	$c/282$	0.041	$L/5854$	0.013	$L/18462$	0.069	0.288
ACF 80 × 80 × 4 – 240 – 3	0.251	$c/318$	0.038	$L/6316$	0.012	$L/20000$	0.072	0.300
ACF 80 × 80 × 4 – 1000 – 1	0.663	$c/121$	0.250	$L/4006$	0.110	$L/9066$	0.627	0.627
ACF 80 × 80 × 4 – 1000 – 2	0.775	$c/103$	0.128	$L/7842$	0.076	$L/13098$	0.306	0.306
ACF 80 × 80 × 4 – 1000 – 3	0.365	$c/219$	0.281	$L/3562$	0.088	$L/11318$	0.317	0.317
ACF 80 × 80 × 4 – 1000 – 4	0.454	$c/176$	0.214	$L/4677$	0.114	$L/8789$	0.302	0.302
ACF 80 × 80 × 4 – 2000 – 1	0.584	$c/137$	0.272	$L/7363$	0.522	$L/3834$	0.478	0.239
ACF 80 × 80 × 4 – 2000 – 2	0.633	$c/126$	0.303	$L/6609$	0.461	$L/4334$	0.730	0.365
ACF 80 × 80 × 4 – 2000 – 3	0.568	$c/141$	0.323	$L/6194$	0.434	$L/4607$	0.451	0.225
ACF 80 × 80 × 4 – 2000 – 4	0.701	$c/114$	0.259	$L/7715$	0.477	$L/4197$	0.643	0.321

As shown in Table 3, the maximum bow imperfection amplitude of the specimens is  $\delta_{v,0} = L/3562$ , whereas the maximum camber imperfection amplitude is  $\delta_{u,0} = L/3834$ . Hence, the amplitudes of initial global geometric imperfections of the tested columns are considerably lower than the maximum fabrication tolerance of  $L/750$  permitted for steel profiles by EN 1090-2 [20]. Additionally, the maximum amplitudes of uniform longitudinal twist,  $\theta_0$ , of all specimens do not exceed 1°/m, which is the allowable twist imperfection applied to cold-formed sections according to EN 10162 [21].

#### 2.4. Stub column tests

The ultimate resistance and deformation capacity of selected angle sections were quantified by stub column tests, which allowed for an impact assessment of cross-section effectiveness on the failure mode of tested slender angle columns. A total of three repeated stub column tests were performed under pure axial compression. The steel sheets were cut into strips and press-braked into angle sections having nominal dimensions 80 x 80 x 4 mm and a nominal internal corner radius of 12 mm. The nominal length of specimens of 240 mm meets requirements in Clause A.3.2.1 of EN 1993-1-3 [22]; this adopted length is considered short enough to preclude global buckling and to contain a representative pattern of local geometric imperfection and residual stress as a more slender member from the same producing stock. The longitudinal axis of the specimens was oriented parallel to the direction of the flat strip rolling. The specimen's length and geometric dimensions, measured prior to stub column testing, are reported in Table 2.



(a) Instrumentation configurations (all dimensions are in mm)

(b) Test setup

**Fig. 6.** Test setup for stub column specimens.

The ends of each stub column were milled flat to allow full contact with the parallel plates of the testing machine. The parallel end plates were fixed against rotations and twist about any axis to achieve fixed boundary conditions. The compressive load was applied using a strain-controlled hydraulic testing machine (Amsler, Switzerland), with a capacity of 3500 kN. The strain rate was  $0.001 \text{ s}^{-1}$ . Four linear variable displacement transducers (LVDTs), placed on the upper plate of the testing machine, were used to monitor the end shortening of the stub columns. Four linear electrical strain gauges (SGs) were attached respectively at a distance of 25 and 5 mm from the section corners and legs' tips, respectively, at specimens' mid-height, to determine the corresponding longitudinal strains, while a load cell was used to record the applied load. All experimental results—load, displacement and strain values—were recorded in one-second intervals on the data acquisition device MGC+ (HBM, Germany). The test setup of stub column specimens is shown in Fig. 6.

The failure of specimens was governed by local buckling. Buckling was localised in the middle part of the specimen height and characterised by torsional deformations of both angle legs. The line junctions between legs remained straight and angles between legs did not change. A typical deformed specimen is shown in Fig.

7.

The end shortening readings measured by the LVDTs were modified using the SG readings to account for the elastic deformation of the end plates of the testing machine, present in the LVDT measurements [23]. Fig. 8 depicts the modified true load–end shortening curves for all the specimens. The key experimental results are summarised in Table 4, in which  $P_{c,u}$  is the ultimate buckling load,  $\sigma_{lb}$  is the LB stress obtained as the ultimate load-to-measured cross-section area ratio of each specimen and  $f_{ya}$  is an enhanced average yield strength which accounts for cold working in press-braked sections, obtained in accordance with [24], [25], using the measured cross-section area of each specimen (Table 2) and the average values of yield strengths for flat and corner tensile coupon tests performed on final press-braked section (Table 1). To quantify the elastic buckling behaviour and strain-hardening effects caused by the cold forming process, the LB stress  $\sigma_{lb}$  is compared with the enhanced average yield strength  $f_{ya}$ . It can be seen from Table 4 that the failure mode of the specimens is governed by elastic LB occurring at a stress value that is considerably lower than the enhanced average yield strength  $f_{ya}$ . It can be concluded that the angle section ACF  $80 \times 80 \times 4$  is susceptible to elastic local instabilities below the yield point and it can be classified as a slender or effective cross-section belonging to Class 4 [12].

**Table 4.** Summary of stub column test results.

Specimen	Ultimate load $P_{c,u}$ (kN)	End shortening at ultimate load $\delta_u$ (mm)	Ultimate buckling stress $\sigma_{lb}$ (N/mm <sup>2</sup> )	Enhanced average yield strength $f_{ya}$ (N/mm <sup>2</sup> )	Comparison $\sigma_{lb} / f_{ya}$
ACF $80 \times 80 \times 4 - 240 - 1$	199.0	1.21	327.7	544.1	0.60
ACF $80 \times 80 \times 4 - 240 - 2$	198.2	1.17	320.2	544.2	0.59
ACF $80 \times 80 \times 4 - 240 - 3$	203.7	0.83	328.7	544.2	0.60
Mean value	200.3	1.1			
Standard deviation	3.0	0.2			
CoV (%)	1.5	19.5			



**Fig. 7.** Stub column failure mode of specimen ACF  $80 \times 80 \times 4 - 240 - 2$ .

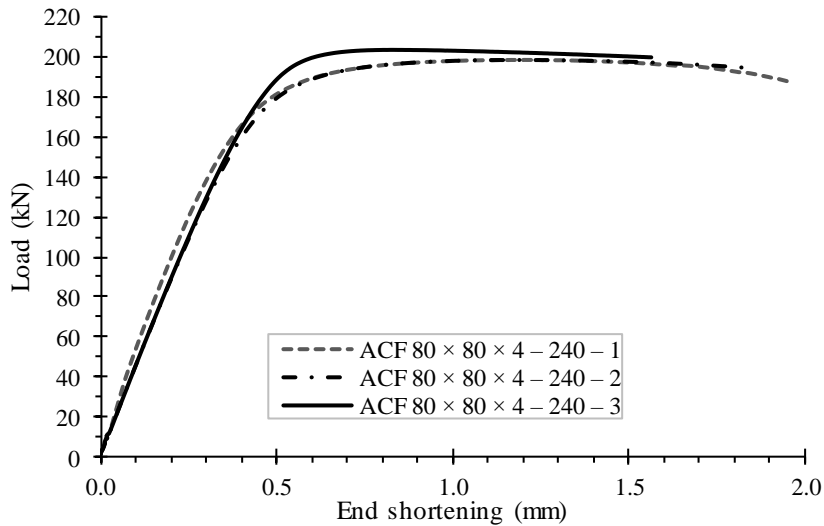


**Fig. 8.** Load–end shortening curves from stub column tests.

## 2.5. Global buckling tests

### 2.5.1. Test setup and procedure

Global buckling tests were performed on pin-ended press-braked stainless steel equal-leg angle columns to study their actual structural responses and identify key predictors for critical failure modes. The experiment included a total of 8 specimens with nominal dimensions  $80 \times 80 \times 4$  mm and nominal internal corner radius of 12 mm. The specimens were divided into two test series with nominal lengths of 1000 and 2000 mm, respectively. To gain reliable data, four repeated tests were included in each series. The specimens were cut to the required lengths by a water jet cutter, ensuring a flat mill of ends and providing full contact with the end plates of the testing machine. Both ends of each specimen were parallel to each other and perpendicular to the column's longitudinal axis. Measurements of specimen geometry and initial global imperfections were subsequently performed and are presented in Table 2 and Table 3, respectively.

The distance between the face of the bearing plate and the axis of rotation was 90 mm at both supports, hence the column effective length  $L_e$  was taken as  $L_e = L + 2 \cdot 90$  mm, where  $L$  is the actual specimen length.

Monotonic, concentric compression loading was applied to each column using a hydraulic testing machine (Amsler, Switzerland) with a capacity of 2000 kN. The load was applied through end plates attached to hardened steel knife-edges designed to allow rotations about the minor-axis, while restraining major-axis rotations as well as twist rotations and warping. To adjust the top and bottom knife-edges, clamps were employed to provide compressive bearing stress between the loading plates and knife-edges and prevent uplift and detachment. Each specimen was carefully geometrically aligned ensuring that the longitudinal axis

and the line of load action coincide. The specimens were positioned so that their minor principal axis coincided with the axis of the knife-edge rotation causing the specimen to bend about the minor principal axis. The sliding steel clamped with slotted holes and bolts was used to enable the specimen to be adjusted in the rig and clamped to the loading plates. To accurately measure the position of the specimen in both directions, a ruler and calliper were provided in the test machine, as illustrated in Fig. 9.

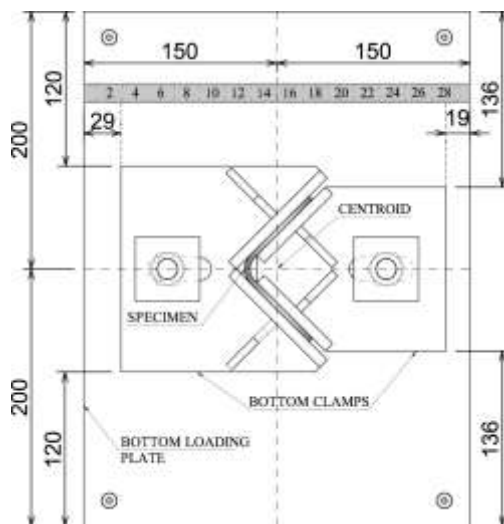


**Fig. 9.** Setting the specimens in the test machine: bottom measuring plate (all dimensions are in mm).

The column test setup was equipped with a series of LVDTs to record the displacements and rotations of the end plates and the specimen throughout the experiment. SGs were used to monitor axial strain readings in order to quantify possible load eccentricity and record the column structural behaviour with progressing load increments. The test setup and mounted instrumentations are illustrated in Fig. 10.

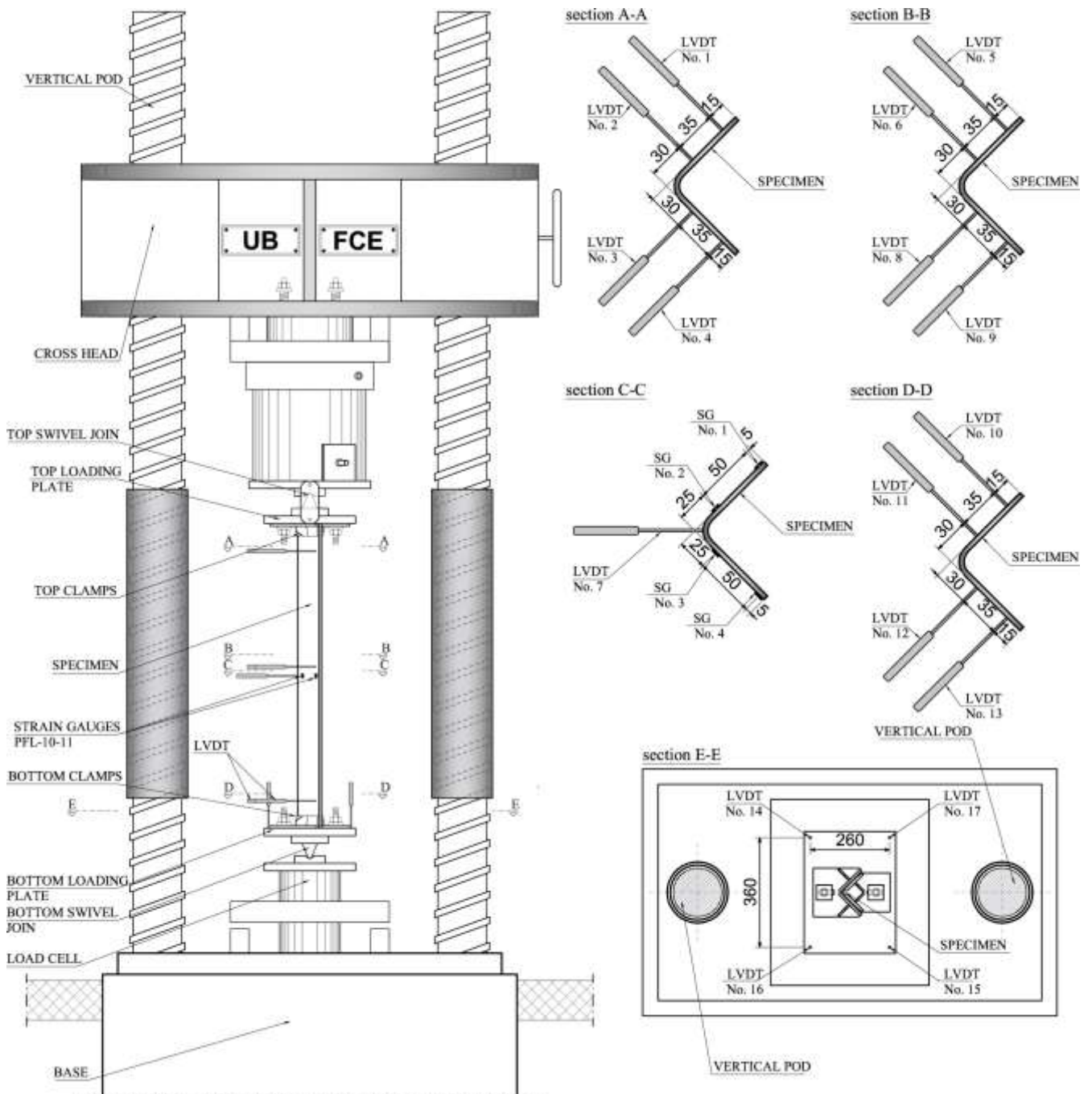


**Fig. 10.** Test setup and instrumentation configuration for global buckling tests (all dimensions are in mm).

Four LVDTs were utilized to record bottom plate rotations and displacements with another four LVDT mounted on each leg of the mid-height cross-section to record its movements and deformations. The displacement in the expected buckling plane perpendicular to the minor principal axis was also measured with an additional LVDT at the mid-height of specimens. Four additional LVDTs were placed at a distance of 200 mm from specimens' ends. Four SGs were attached around the perimeter surface of the cross-section at the specimens' mid-height near leg tips and angle corners.

The results were used to calculate several parameters such as cross-section lateral displacements in the minor and major-axis directions, cross-section torsional rotation, and leg LB. A calibrated load cell C6A Force

Transducer (HBM, Germany) was used to measure the applied load. A data acquisition system was used to record the applied load, LVDTs and SGs readings during the tests. After aligning the specimens, all tests were performed under displacement control with a load rate not exceeding 0.01 mm/s up to the maximum load capacity, and then continued up to approximately 70% of the maximum load before the test was stopped.

### 2.5.2. Test results

Typical deformed shapes of specimens ACF  $80 \times 80 \times 4 - 1000$  and ACF  $80 \times 80 \times 4 - 2000$  after buckling are shown in Fig. 11 and Fig. 12, respectively.

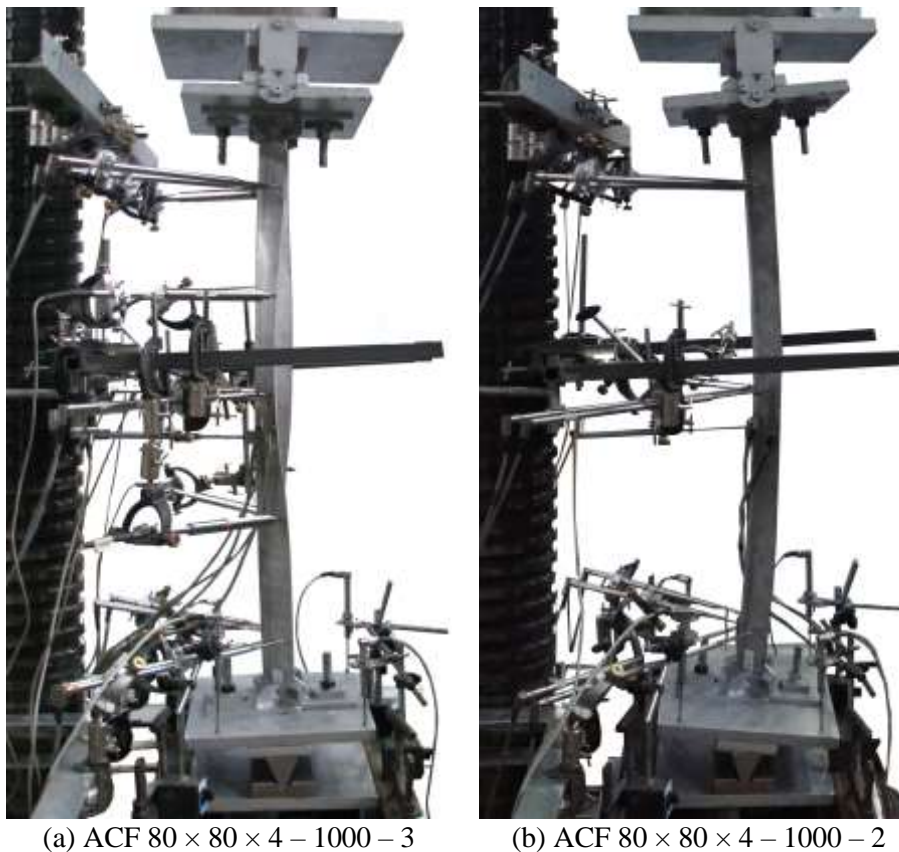
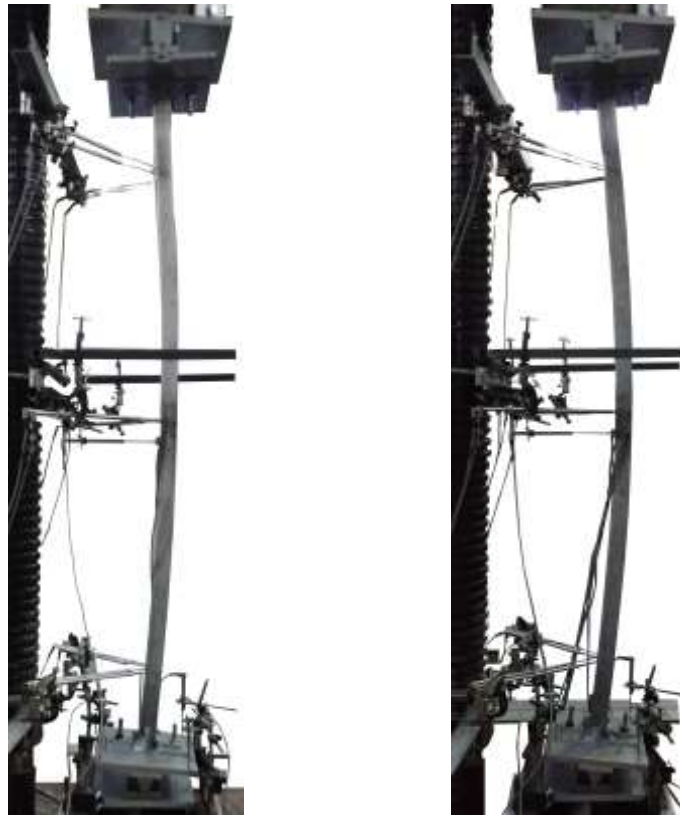


**Fig. 11.** Typical failure modes of specimens in series ACF  $80 \times 80 \times 4 - 1000$ .



(a) ACF  $80 \times 80 \times 4 - 2000 - 1$  (b) ACF  $80 \times 80 \times 4 - 2000 - 4$

**Fig. 12.** Typical failure modes of specimens in series ACF  $80 \times 80 \times 4 - 2000$ .

Key experimental results presented in graphical form as load–lateral deflection about minor-axis curves, load–torsional rotation curves and load–axial strain curves are shown in Fig. 13 to Fig. 16, developed for mid-height of selected specimens.

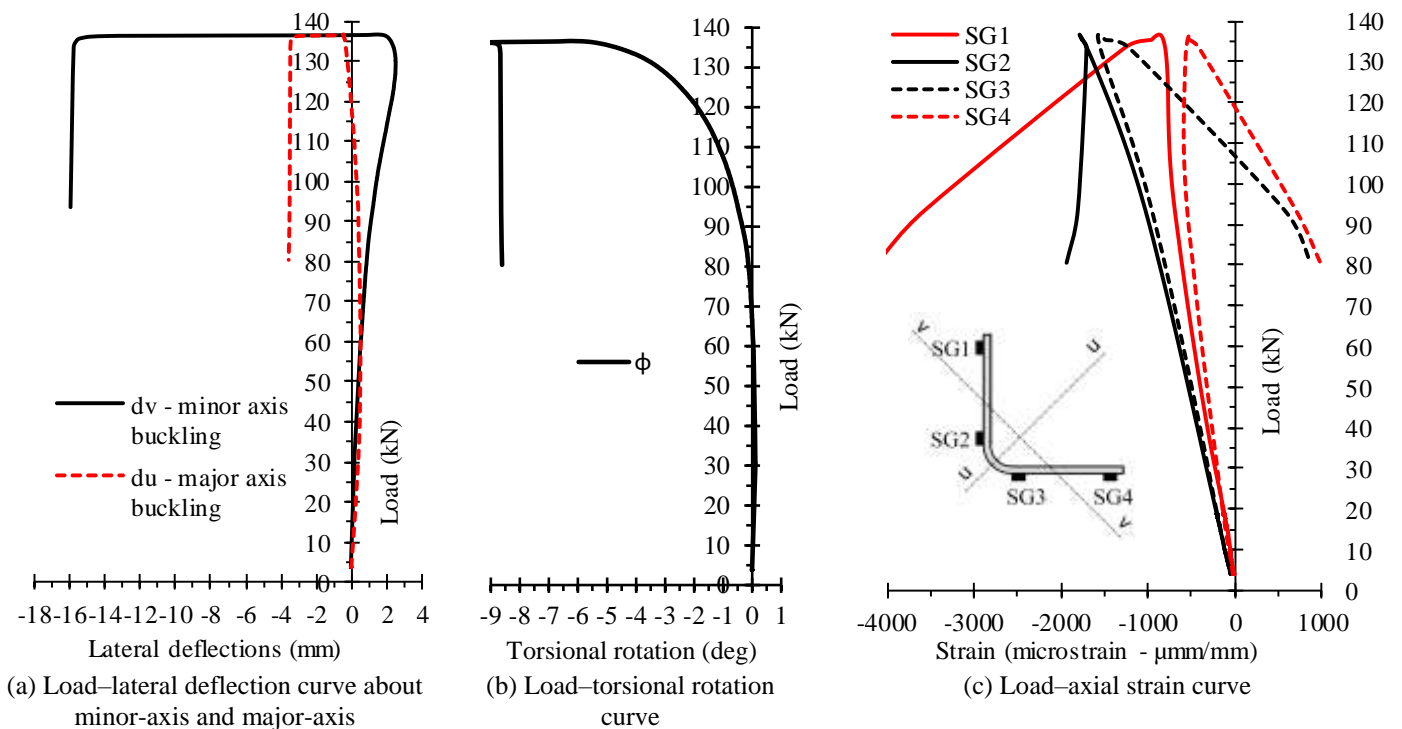


**Fig. 13.** Curves of global buckling test at mid-height of specimen ACF  $80 \times 80 \times 4 - 1000 - 3$ .

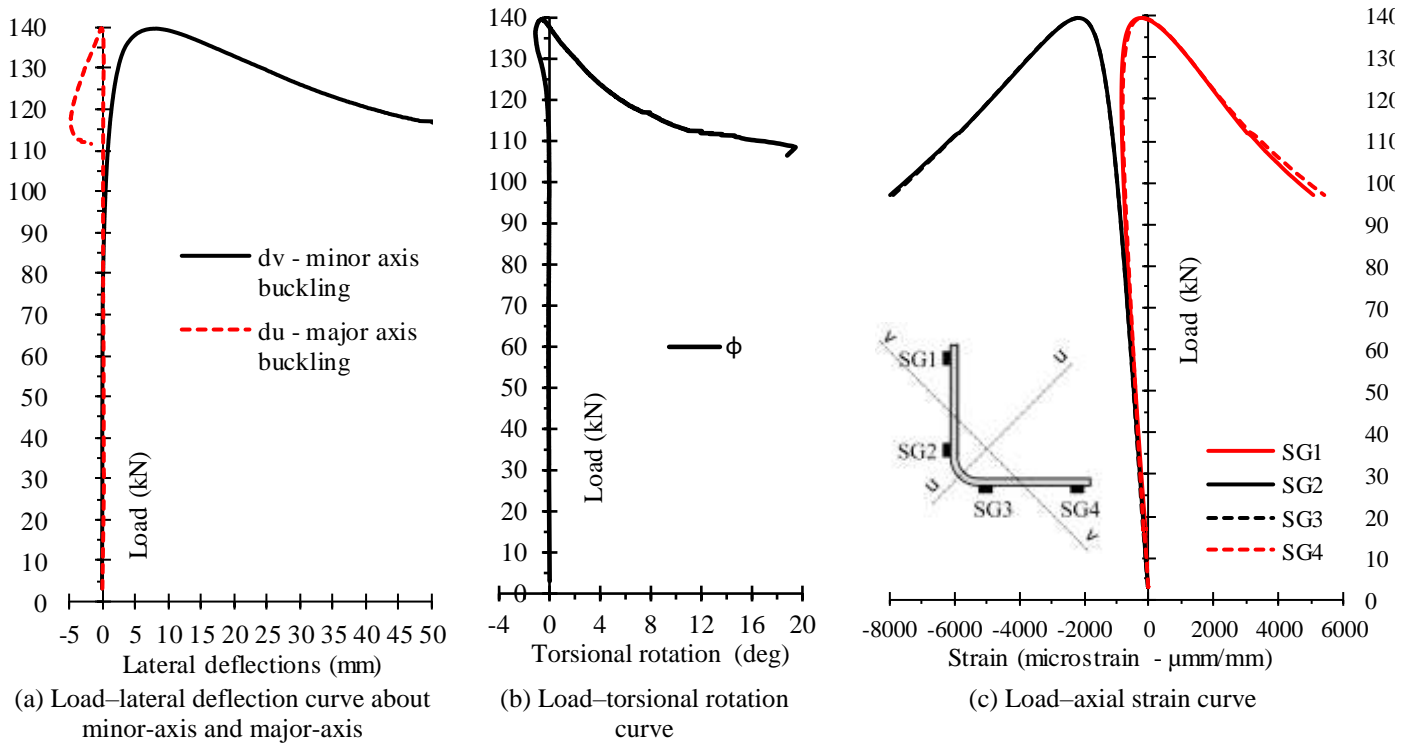


**Fig. 14.** Curves of global buckling test at mid-height of specimen ACF  $80 \times 80 \times 4 - 1000 - 2$ .

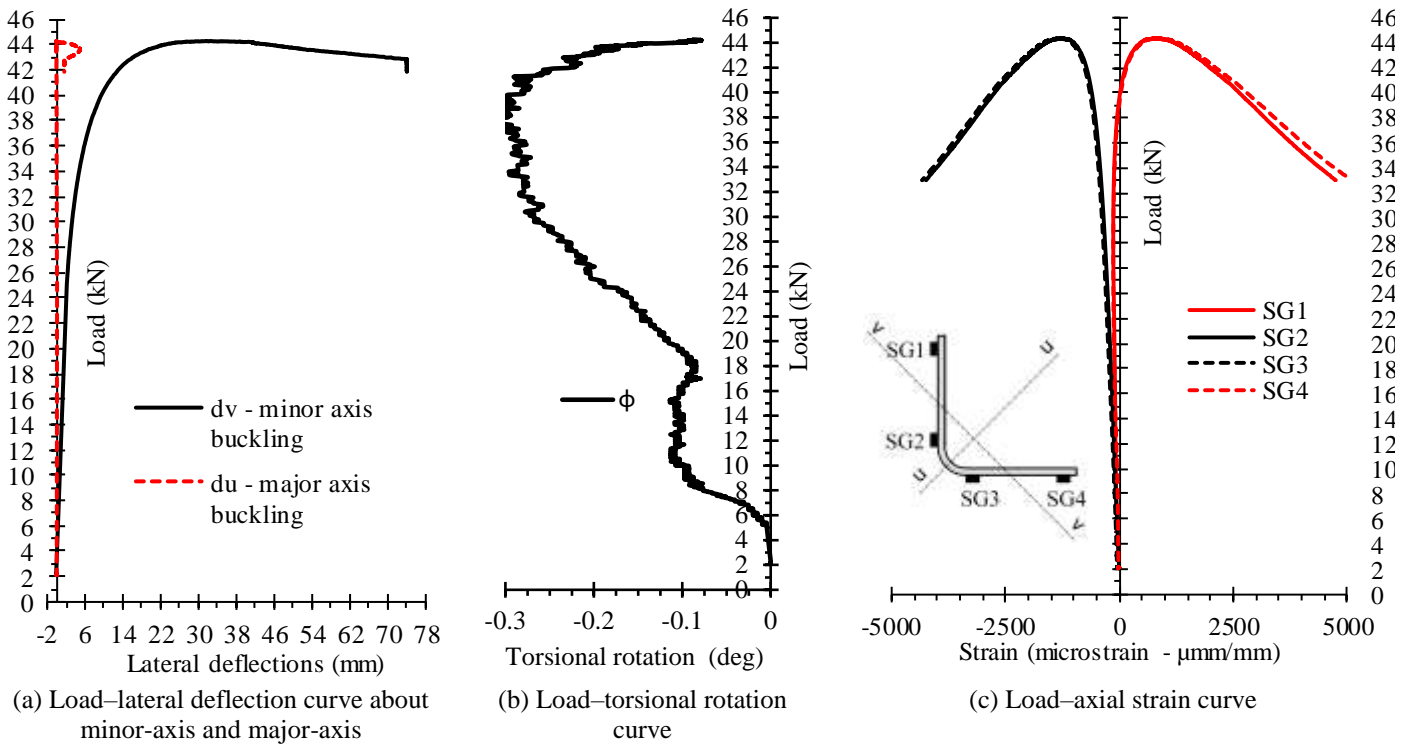


**Fig. 15.** Curves of global buckling test at mid-height of specimen ACF  $80 \times 80 \times 4 - 2000 - 1$ .

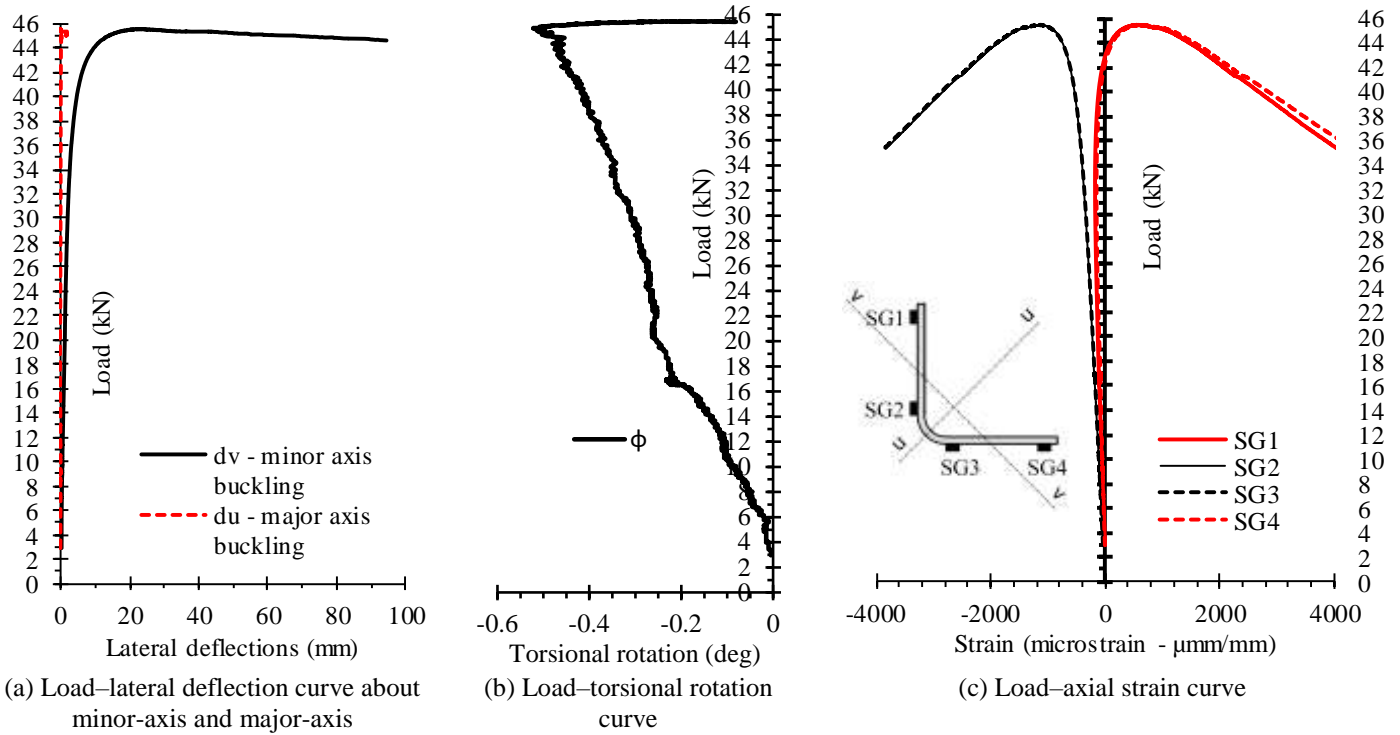


**Fig. 16.** Curves of global buckling test at mid-height of specimen ACF 80 × 80 × 4 – 2000 – 4.

The lateral deflections about the cross-section geometric axes  $d_x$  and  $d_y$ , lateral deflections about the cross-section major and minor principal axes  $d_u$  and  $d_v$  and distribution of torsional rotations  $\phi$ , were obtained following procedure described by Landesmann et al. (2017) [9] and illustrated in Fig. 17.

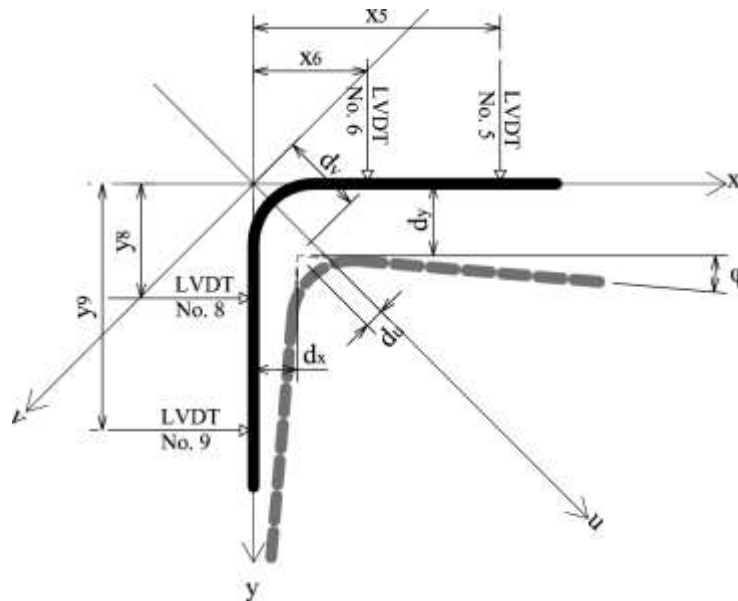


**Fig. 17.** Cross-section undeformed and deformed configuration (numerical designations are consistent with LVDT designations placed at specimen mid-height).

Fig. 17 shows an undeformed (reference) angle section in the X–Y coordinate system and its deformed configuration in the U–V coordinate system. Along with cross-sections, the locations of the four LVDTs placed perpendicular to the angle legs at distances  $x_5 = 65$  mm,  $x_6 = 30$  mm and  $y_8 = 30$  mm,  $y_9 = 65$  mm from the corner, are also depicted. The deviation of the section deformed configuration from its initial

reference position is indicated by LVDTs readings. The signs of the LVDTs displacement measurements are in accordance with the  $x, y$  (X – Y plane) and  $u, v$  axes (U – V plane), whereas the torsional rotations  $\varphi$  are positive clockwise.

The cross-section torsional rotation  $\varphi$  may be determined from one of the following equations:

$$\varphi = \tan^{-1} \left( \frac{l_9 - l_8}{y_9 - y_8} \right) \quad \text{or} \quad \varphi = \tan^{-1} \left( \frac{l_5 - l_6}{x_5 - x_6} \right) \quad (1)$$

where  $l_5, l_6, l_8$  and  $l_9$  are the readings of LVDT5, LVDT6, LVDT8 and LVDT9, respectively.

The values of  $d_x$  and  $d_y$ , defining the location of the deformed cross-section corner and referring to the cross-section geometric axes, can be expressed as

$$d_x = (l_9 \tan \varphi + l_5 + y_9 \tan^2 \varphi - x_5 \tan \varphi) / (1 + \tan^2 \varphi) \quad (2)$$

$$d_y = (l_9 - l_5 \tan \varphi + y_9 \tan \varphi + x_5 \tan^2 \varphi) / (1 + \tan^2 \varphi) \quad (3)$$

The location of the deformed cross-section corner along the cross-section principal axes  $d_u$  and  $d_v$ , is found as follows:

$$d_u = (d_y - d_x) / \sqrt{2} \quad (4)$$

$$d_v = (d_x + d_y) / \sqrt{2} \quad (5)$$

Table 5 provides all relevant data for both specimen series;  $P_{b,u,exp}$  is the maximum axial load capacity of the specimens (failure load),  $d_{u,v}$  and  $d_{u,u}$  are the mid-height lateral deflections about minor and major principal axes, respectively, corresponding to the failure load and  $\varphi_u$  is the mid-height torsional rotation corresponding to the failure load. Table 5 also lists the characteristic values,  $R_k$ , of ultimate buckling loads  $P_{b,u}$  for each tested group, determined on the basis of a statistical evaluation in accordance with Annex D, EN 1990:2002 [26].

**Table 5.** Summary of global buckling test results.

Specimen	Failure mode	$P_{b,u,exp}$ (kN)	$d_{u,u}$ (mm)	$d_{u,v}$ (mm)	$\varphi_u$ (deg)
ACF $80 \times 80 \times 4 - 1000 - 1$	FTB+LB+FB	132.5	+0.335	+0.339	-8.013
ACF $80 \times 80 \times 4 - 1000 - 2$	FB+LB+ FTB	139.5	-0.156	+8.149	-0.613
ACF $80 \times 80 \times 4 - 1000 - 3$	FTB+LB+FB	136.6	-0.468	+1.471	-6.234
ACF $80 \times 80 \times 4 - 1000 - 4$	FTB+LB+FB	135.5	-0.288	+0.846	-8.060
Mean value		136.0			
Standard deviation		2.90			
CoV (%)		2.13			
$R_k$ (EN 1990 Ann. D)		128.4			
ACF $80 \times 80 \times 4 - 2000 - 1$	FB	44.3	-0.053	+31.487	-0.103
ACF $80 \times 80 \times 4 - 2000 - 2$	FB	45.8	+0.229	+23.948	-0.274
ACF $80 \times 80 \times 4 - 2000 - 3$	FB	46.8	-1.132	+29.094	+0.987
ACF $80 \times 80 \times 4 - 2000 - 4$	FB	45.5	-0.023	+21.972	-0.204
Mean value		45.6			
Standard deviation		1.03			
CoV (%)		2.26			
$R_k$ (EN 1990 Ann. D)		42.9			

### 3. Discussion

#### 3.1. Discussion of experimental results

Based on experimental data obtained for global buckling tests, the following conclusions can be drawn:

1) Intermediate length specimens: ACF  $80 \times 80 \times 4 - 1000$  ( $L = 1000$  mm)

In this tested series, three specimens (denoted as 1, 3 and 4 in repeated tests) failed in an almost identical mode, exhibiting dominant major-axis flexural-torsional deformations, coupled with minor-axis FB and LB, as displayed in Fig. 11a. However, the ultimate buckling mode is predominantly torsional with twist rotations significantly greater than both major and minor-axis flexural displacements (see Table 5). The experimental responses: axial load vs. torsional rotations ( $P-\varphi$ ), axial load vs. lateral deflections due to major-axis FB ( $P-d_u$ ) and axial load vs. lateral deflections due to minor-axis FB ( $P-d_v$ ) indicate the same trend with gradual growth characterized by a change in sign through the loading phase up to onset of FTB when the compressive capacity of the specimen reaches the maximum value (see Fig. 13a and Fig. 13b). Fig. 13a also shows a relatively uniform trend of column strength in the buckling regime followed by significant growth of lateral deflections in the major-axis direction (minor-axis buckling). The response eventually results in a sudden failure with a significant reduction of column capacity. The considerably higher minor-axis flexural displacements in comparison with their major-axis counterparts are probably attributable to the influence of effective centroid shift (shifting of the neutral axis upon local cross-section buckling) and interaction with minor-axis FB, relevant for columns with relatively close FTB and FB loads.

The distribution of longitudinal strains demonstrates a uniform application of the compression load into the critical cross-section in the early loading phase. The gradual separation of ascending branches (quite symmetric relative to the major-axis) of the load–axial strain response indicates the appearance of leg bending in both directions of principal section axes (see Fig. 13c). When the ultimate buckling load was reached, all elements of the cross-section were compressed. In the descending post-buckling path, due to bi-axial bending, compressive strains occur in one leg and tensile strains occur in the other leg of the angle section.

In contrast to these specimens, the dominant failure mode of specimen ACF  $80 \times 80 \times 4 - 1000 - 2$  (see Fig. 11b) was the interaction of global FB about the minor-axis and local cross-section buckling accompanied by significant lateral minor-axis displacements and negligible major-axis bending and torsional effects (see Table 5). As shown in Fig. 14a, the axial load vs. lateral minor-axis deflections ( $P-d_v$ ) equilibrium path is smooth with gradual branching. The positive readings for lateral deflections  $d_v$  in the peak and post-peak regimes imply minor-axis FB deformations in a direction towards the leg tips, see Fig. 11b. The minor-axis FB features of specimen ACF  $80 \times 80 \times 4 - 1000 - 2$  differ from those found in other repeated tests (denoted as 1, 3 and 4), in which lateral deflections  $d_v$  were measured as having a negative sign in the post-peak regime (i.e. minor-axis FB deformations were in a direction towards the angle corner), see Fig. 11a and Fig. 13a. The compressive capacity of tested column reaches the maximum at the onset of FB and then gradually diminishes as growth of lateral deflections takes place. The ascending part of axial load vs. lateral major-axis deflection curve ( $P-d_u$ ) branches out of the null displacement vertical line at a quite high loading stage (see Fig. 14a). However, in the peak load stage, even very slight major-axis bending leads to the appearance of torsional deformations which dramatically increase after reaching the peak load and specimen failure (see Fig. 14b), indicating the sensitivity of the specimen to FTB and the elastic LB of the cross-section. The axial load vs. axial strain response, shown in Fig. 14c, also confirms the observed minor-axis FB pattern. At the peak load regime, the compressive strains are noticed in the entire angle section. By further increasing the lateral deflections—followed by a drop of the specimen’s strength—tensile strains occurred at the legs’ tips and compressive strains at the section corner region. Such structural response of specimen ACF  $80 \times 80 \times 4 - 1000 - 2$  is probably affected by initial load eccentricity towards the corner in the major-axis direction

relative to the section centroid, which slightly increases its compressive strength compared with the strengths of the remaining three specimens (denoted as 1, 3 and 4) which dominantly failed in FTB (see Table 5).

Despite different governing modes in the intermediate length test series, the ultimate buckling loads of all specimens are quite similar, ranging from 132.5 to 139.5 kN, with a mean value of 136.0 kN and standard deviation of 2.9 kN. The characteristic value of the buckling resistance is 128.4 kN.

2) Long specimens: ACF  $80 \times 80 \times 4 - 2000$  ( $L = 2000$  mm)

As shown in Fig. 12, a characteristic failure mode of the long specimens was global minor-axis FB. The recorded responses ( $P-d_v$ ), ( $P-d_u$ ) and ( $P-\phi$ ), presented in Fig. 15a and Fig. 15b for specimen ACF  $80 \times 80 \times 4 - 2000 - 1$ , and in Fig. 16a and Fig. 16b for specimen ACF  $80 \times 80 \times 4 - 2000 - 4$ , indicate that the failure pattern involves notable lateral deflections in plane perpendicular to the minor principal axis and negligible twisting in combination with major-axis bending (almost null values in loading and peak load regime). This reflects the fact that the high slenderness specimens are less prone to cross-section LB. The observed buckling mode is additionally confirmed by the equilibrium path shape recorded by SGs, shown in Fig. 15c and Fig. 16c. The distribution of axial strains represents a symmetric deflected mode, with the curves that gradually separate as the applied load and lateral minor-axis deflections increase. At the ultimate load level and in the post-buckling regime that is followed by a drop of the specimen's load capacity, tensile strains occurred at the legs' tips and compressive strains at the corner region (bending towards the legs' tips). Such distributions of axial stresses along the cross-sections of long length specimens are probably triggered by the initial bow imperfections of the specimens that bend towards the leg tip direction, and by initial load eccentricity towards the angle corner in the major-axis direction. The application of increased compression in the angle corner reduces the stress level at the leg tips leading to higher column compressive capacity than in the case of minor-axis FB towards the angle corner [2]. The failure loads of specimens ranged from 44.0 to 46.4 kN, with a mean value of 45.2 kN and standard deviation of 1.0 kN. The characteristic value of the buckling resistance is 42.9 kN.

### 3.2. Comparisons with design predictions

In this section, procedures for the design of stainless steel equal-leg angle columns given in European standard EN 1993-1-4 [12], Design Manual for Structural Stainless Steel (DMSSS) [25] and Australian/New

Zealand standard AS/NZS 4673 [14] are briefly summarised and then quantitatively evaluated by comparing experimentally obtained load capacity  $P_{u,exp}$  (mean value for each tested series) with the unfactored design capacity predictions  $P_{u,pred}$ .

The mentioned specifications permit the use of an EWM in the design of compressed thin-walled members having cross-section plate elements with width-to-thickness ratios greater than the limits for full effectiveness. This method accounts for local buckling and cross-section post-buckling strength through the reduction of each plate comprising a cross-section to an effective plate. The calculation method used to determine the effective width of the plate elements introduces a reduction factor, which depends on the plate support conditions, loading conditions, yield strength of the material and plate width-to-thickness ratio.

The calculation method given in EN 1993-1-4 [12], Clause 5.4 for the cross-section capacity of CFSS sections is based on the method for carbon steel provided in EN 1993-1-5 [27] but prescribes more conservative expressions for reduction factors to allow for stainless steel material non-linearity. If the slenderness width-to-thickness ratio  $c/t$  (for cold-formed angle  $c$  is the notional flat leg width, measured from the midpoint of the corner up to the free end, and  $t$  is the leg thickness) of the equal-leg angle is larger than  $14 \cdot \varepsilon$  ( $\varepsilon$  is the material parameter), the cross-section compressive capacity should be reduced due to LB. The effective width of a uniformly compressed angle leg (outstand plate element), positioned at its supported end, is determined using a plate buckling coefficient of 0.43.

In accordance with EN 1993-1-1 [28], the design approach for carbon steel members centrically subject to axial compression, is based on the Perry-Robertson buckling curve and uses a linear expression for the imperfection parameter  $\eta = \alpha(\bar{\lambda} - \bar{\lambda}_0)$ . The influences of geometric imperfections, residual stresses and load eccentricity on the predicted FB resistance is implicitly accounted for by employing an imperfection factor  $\alpha$  associated with the appropriate buckling curve depending on the cross-section shape and manufacturing process. However, the supplementary rules provided in EN 1993-1-4 [12] do not explicitly state the values of the imperfection factor  $\alpha$  nor the limiting slenderness  $\bar{\lambda}_0$  for stainless steel angles in the relevant buckling plane depending both on the manufacturing process and stainless steel grade. Instead, only three design curves are specified: the parameters  $\alpha$  and  $\bar{\lambda}_0$  are equal to 0.49 and 0.40, respectively, for FB of cold-formed open cross-sections, 0.76 and 0.20, respectively, for FB of welded sections, whereas for torsional and FTB,

they are equal 0.34 and 0.20, respectively. However, based on research findings conducted over the last decade, the fourth edition of the DMSSS [25] revised the buckling curves for FB and adopted the more conservative curve ( $\alpha = 0.76$ ,  $\bar{\lambda}_0 = 0.2$ ) for FB for CFSS angle sections.

Single angles loaded through one leg fail by interaction between the axial force and biaxial bending. The design procedure stated in Annex BB of EN 1993-1-1 [28] treats this interaction by adopting a non-dimensional effective (modified) slenderness ratio instead of a geometrical one in the Perry-Robertson formulae (the load eccentricities may be neglected) under the condition that both ends of the column are welded or connected by at least two bolts. When only one bolt is used for end connections, the angle columns should be designed for the actual end eccentricities using the appropriate interaction equations. Besides, for columns with non-symmetric slender (Class 4) cross-sections, allowance shall be made for the additional moment due to the eccentricity of the centroid of the effective cross-section with respect to the centroid of the gross cross-section. Angle sections subject to combined axial compression and additional bending moment should satisfy the criterion (6.25) provided in Clause 6.1.9 of EN 1993-1-3 [22]. To account for interaction between global major-axis FTB or minor-axis FB and the effective centroid shift effects (LB), interaction formula (5.15) provided in Clause 5.5 of EN1993-1-4 [12] should be used for the design of stainless steel equal-leg angle columns that are initially axially compressed.

Clauses 2.2 and 2.3 of the Australian standard for cold-formed stainless steel structures AS/NZS 4673 [14], which is based on the American standard SEI/ASCE-8 [13], adopt provisions from the AISI Specification for cold-formed carbon steel [29] for determining the reduction factors for stiffened and unstiffened elements, uniformly compressed and with stress gradients (Winter's plate buckling curves). The plate buckling coefficient of 0.5 is taken for uniformly compressed unstiffened elements compared with a value of 0.43 used in EN 1993-1-4. Unlike the EN 1993-1-5 [27], there are no rules for calculating the plate buckling coefficient for unstiffened elements subject to a stress gradient.

The centrally compressed stainless steel columns may be designed using the tangent-modulus approach which accounts for the material nonlinearity and gradual yielding of stainless steel. The procedure for FB, Clause 3.4.2, employs the Euler formula in which the initial elastic modulus is replaced with the tangent modulus corresponding to the buckling stress which involves an iterative design procedure. The predictive

expressions for torsional and flexural-torsional buckling resistance, given in Clauses 3.4.3 and 3.4.4 also introduce the tangent modulus.

In addition to the iterative tangent method, the Australian standard also allows the column strength to be determined using the explicit method developed by Rasmussen and Rondal [30], [31]. This method involves using the Perry-Robertson formulas with the modified imperfection parameter  $\eta = \alpha \left( (\bar{\lambda} - \bar{\lambda}_1)^\beta - \bar{\lambda}_0 \right)$  to produce strength curves for columns made from different stainless steel grades. It involves the material constants  $\alpha$ ,  $\beta$ ,  $\bar{\lambda}_0$ , and  $\bar{\lambda}_1$ .

In accordance with AS/NZS 4673 [14], the angle section columns subjected to concentric compression should be designed as beam-columns under eccentric compression introducing the additional bending moment of  $P \cdot L / 1000$  about the minor principal axis that causes compressive stress in the leg tips. This requirement refers to both slender and non-slender angle sections. To satisfy these criteria, the interaction formulae 3.5 (1) and 3.5 (2) described in Clause 3.5 should be used.

The accuracy of the mentioned design provisions [12], [14] for pin-ended CFSS equal-leg angle section columns was assessed through comparisons against the test data  $P_{u,exp}$  (mean value for each tested series). The design capacity predictions  $P_{u,pred}$  were based on the enhanced average yield strength of the cross-section [24],[25], i.e., including the corner strength enhancement. To evaluate the influence of the shift of the centroid when considering the effective cross-section, the design resistances were obtained using the interaction formulae. The direction of the predicted shift in the equal-leg angle section leads to a secondary minor-axis bending moment with no secondary major-axis bending moment. A shift of the effective centroid towards the section corner causes bending towards the corner (compressive stresses at the leg tips). Table 6 reports the  $P_{u,exp}/P_{u,pred}$  ratios for each design procedure.

**Table 6.** Comparisons of experimental results with predicted strengths.

Specimen			EN 1993-1-4	DMSSS	AS/NZS 4673
	Failure mode nature	Non-dimensional slenderness $\bar{\lambda}_p$	$P_{u,exp} / P_{u,pred}$	$P_{u,exp} / P_{u,pred}$	$P_{u,exp} / P_{u,pred}$
ACF 80 × 80 × 4 – 240	LB	0.189	4.42	4.42	3.27
ACF 80 × 80 × 4 – 1000	FTB+LB+FB	0.929	4.98	4.98	3.16
ACF 80 × 80 × 4 – 2000	FB	1.717	2.58	2.80	1.78

Summing up the comparison results, it is found that the European and Australian/New Zealand standards provide adequate predictions of failure modes both for specimens of low, intermediate and high slenderness.

The use of codified procedures leads to safe but significantly conservative predictions for LB, FTB and FB resistances. However, a comparison with the test results presented in Table 6 reveals that AS/NZS 4673 offers a higher level of design accuracy than EN 1993-1-4. The experimental-to-design cross-section resistance is 4.42 and 3.27 for EN 1993-1-4 and AS/NZS 4673, respectively. Considering FTB, the experiment-to-design ratio is equal to 4.98 for EN 1993-1-4 and 3.16 for AS/NZS 4673. In the case of long length specimens, better correlation in predictions of minor-axis FB resistance was again found for AS/NZS 4673, with an experiment-to-design ratio of 1.78 in comparison with values of 2.58 and 2.80 obtained using EN 1993-1-4 and DMSSS, respectively.

#### **4. Conclusions**

The structural behaviour and load-carrying capacities of pin-ended cold-formed stainless steel angle columns susceptible to LB, FTB and minor-axis FB were experimentally investigated in the paper. The experimental programme was carried out on plain press-braked lean duplex stainless steel (EN 1.4162) equal-leg angle columns with nominal section dimensions of  $80 \times 80 \times 4$  mm and lengths of 240, 1000 and 2000 mm. To obtain reliable and qualitative results, four repeated tests were performed in each specimen series. The experiments involved material tensile coupon tests, initial imperfection measurements, stub column tests and global buckling tests. The investigation fills the gap created by the lack of experimental results and the consequent absence of explicit design guidelines for CFSS equal-leg angle columns in European standard. Based on experimental findings, the following conclusions can be drawn:

- The measured yield strength of lean duplex stainless steel exceeds the nominal value in the product standard by a margin of 12.5%. Significant improvement of material strength occurred in the corner region of the angle section due to press-braking; the measured yield strength in the corner regions was 38% higher than the yield strength of the base flat sheet material.
- The failure mode of the short equal-leg angle columns (stub column test) was governed by elastic local buckling, akin to TB, which occurred at a stress value that is 40% lower than the measured average yield strength.
- Elastic FTB coupled with LB and minor-axis FB was the critical failure mode for three repeated specimens in the intermediate slenderness domain. However, one specimen of the same tested series

failed by the interaction of minor-axis FB and LB including negligible FTB. The minor-axis FB features of this specimen were probably triggered by initial loading eccentricity towards the angle corner in the major-axis direction.

- In the high slenderness domain, the failure mode of all specimens was minor-axis FB. The overall FB deformations of all specimens were in a direction towards the leg tips, which increased compressive stresses at the corner region and reduced stresses at the legs' tips. The structural responses of the long length specimens were probably affected by their initial bow imperfections with distributions towards the legs' tips and initial load eccentricities towards the angle corner. The test results also suggest that the specimens were not prone to LB.
- Comparing the experimental results to the current EN 1993-1-4 and AS/NZS 4673 specifications indicates that stated design procedures, including interactive formulae in conjunction with the EWM and suitable buckling curves, offer safe but inaccurate strength predictions of the tested columns. However, the database developed by the experiments is limited and does not enable a comprehensive assessment of the codified procedures to be undertaken. There is clearly a need to carry out a programme of finite element modelling and parametric studies in order to assess the suitability of the current design provisions for a wider range of geometries than those studied experimentally.

## **Funding**

This investigation is supported by the Serbian Ministry of Education, Science and Technological Development through the TR-36048 project.

## **Acknowledgements**

The authors are grateful to companies Montanstahl ag Switzerland, Vetroelektrane Balkana Belgrade, Armont SP Belgrade, Institute for Testing of Materials Belgrade, Institute for Materials and Structures Faculty of Civil Engineering University of Belgrade, ConPro Novi Sad, Energoprojekt Industrija PLC Belgrade, Vekom Geo Belgrade, CO-Designing, Peri Oplate Belgrade, North Engineering Subotica, Amiga Kraljevo, Mašinoprojekt koprings PLC Belgrade, Sika Belgrade, DvaD Solutions Belgrade and Soko Inženjering Belgrade for their support.

## References

- [1] T.B. Peköz, Development of a Unified Approach to the Design of Cold-Formed Steel Members, Report SG-86-4, American Iron and Steel Institute, 1986.
- [2] Popovic D, Hancock GJ, Rasmussen KJR. Axial compression tests of cold-formed angles. *J Struct Eng (ASCE)* 1999;125(5):515–523.
- [3] Popovic D, Hancock GJ, Rasmussen KJR. Compression tests on cold-formed angles loaded parallel with a leg. *J Struct Eng (ASCE)* 2001;127(6):600–607.
- [4] Young B. Tests and design of fixed-ended cold-formed steel plain angle columns. *J Struct Eng (ASCE)* 2004;130(12):1931–40.
- [5] Ellobody E, Young B. Behavior of cold-formed steel plain angle columns. *J Struct Eng (ASCE)* 2005;131(3):457–66.
- [6] Rasmussen KJR. Design of angle columns with locally unstable legs. *J Struct Eng (ASCE)* 2005;131(10):1553–60.
- [7] Chodraui GMB, Shifferaw Y, Malite M, Schafer BW. Cold-formed steel angles under axial compression. In: LaBoube R, Yu WW, editors. *Proceedings of 18<sup>th</sup> International Specialty Conference on Cold-Formed Steel Structures*. Orlando, Florida, USA, October 27 — 28, 2006:285–300.
- [8] Dinis PB, Camotim D. A novel DSM-based approach for the rational design of fixed-ended and pin-ended short-to-intermediate thin-walled angle columns. *Thin-Walled Struct* 2015;87(February):158–82.
- [9] Landesmann A, Camotim D, Dinis PB, Cruz R. Short-to-intermediate slender pinended cold-formed steel equal-leg angle columns: experimental investigation, numerical simulations and DSM design. *Eng Struct* 2017;132:471–93.
- [10] Kuwamura H, *Local Buckling of Thin-Walled Stainless Steel Members*, *Steel Structures*, 2003;3:191-201.
- [11] Zhang L, Hai Tan K, Zhao O. Experimental and numerical studies of fixed-ended cold-formed stainless steel equal-leg angle section columns. *Thin-Walled Struct* 2019;184:134–144.
- [12] Eurocode 3: Design of steel structures – Part 1-4: General rules – supplementary rules for stainless steels, including amendment A1 (2015), EN 1993-1-4:2006+A1:2015, Brussels, Belgium, CEN 2015.

- [13] SEI/ASCE 8-02: Specification for the Design of Cold-Formed Stainless Steel Structural Members, American Society of Civil Engineers, 2003.
- [14] AS/NZS 4673:2001: Cold-formed stainless steel structures. Australian – New Zealand Standard. Standards Australia, 2001.
- [15] Filipović A, Dobrić J, Marković Z, Baddoo N, Spremić M, Fric N. Experimental investigation of compressed stainless steel angle columns. SDSS 2019 - International Colloquium on Stability and Ductility of Steel Structures. Prague, Czech Republic, 11 — 13 September, 2019.
- [16] Filipović A, Dobrić J, Marković Z, Baddoo N, Flajs Ž. Buckling resistance of stainless steel angle columns. *Gradjevinar* 2019;71(7):547-558.
- [17] EN 10088-4: Stainless steels - Part 4: Technical delivery conditions for sheet/plate and strip of corrosion resisting steels for construction purposes. Brussels, Belgium, CEN 2009.
- [18] EN ISO 6892-1. Metallic materials – Tensile testing. Part 1: Method of test at room temperature. Brussels, Belgium, CEN 2009.
- [19] Arrayago I, Real E, Gardner L. Description of stress-strain curves for stainless steel alloys. *Materials and Design*. 2015;87:540-552.
- [20] EN 1090-2: Execution of steel structures and aluminium structures – Part 2: Technical requirements for steel structures. Brussels, Belgium, CEN 2008.
- [21] EN 10162: Cold rolled steel sections – Technical delivery conditions – Dimensional and cross-sectional tolerances. Brussels, Belgium, CEN 2003.
- [22] Eurocode 3: Design of Steel Structures – Part 1-3: General rules - Supplementary rules for cold-formed members and sheeting EN 1993-1-3, Brussels, Belgium, CEN 2006.
- [23] Gardner L, Nethercot DA. Experiments on stainless steel hollow sections – Part 1: Material and cross-sectional behaviour. *J Construct Steel Res* 2004;60(9):1291–318.
- [24] Rossi B, Afshan S, Gardner L. Strength enhancements in cold-formed structural sections – Part II: Predictive models. *J Construct Steel Res* 2013;83:189–196.

- [25] Afshan S, Arrayago I, Baddoo N, Gardner L, Gedge G, Jandera M, Real E, Rossi B, Stranghöner N, Zhao O. Design manual for structural stainless steel. Fourth Edition Berkshire: The Steel Construction Institute, 2017.
- [26] Eurocode: Basis of structural design EN 1990, Brussels, Belgium, CEN 2002.
- [27] Eurocode 3: Design of steel structures – Part 1-5: Plated structural elements EN 1993-1-5, Brussels, Belgium, CEN 2006.
- [28] Eurocode 3: Design of steel structures – Part 1-1: General rules and rules for buildings EN 1993-1-1, Brussels, Belgium, CEN 2005.
- [29] AISI-S100-16 (2016), North American Specification for the Design of Cold-Formed Steel Structural Members, AISI Standard, American iron and Steel Institute.
- [30] Rasmussen K.J.R, Rondal J, Column curves for stainless steel alloys. J Construct Steel Res 2000;54:89–107.
- [31] Rasmussen K. J. R, Rondal J, Explicit Approach to Design of Stainless Steel Columns. J Struct Eng (ASCE) 1997;123(7):857-863.